

See discussions, stats, and author profiles for this publication at: <https://www.researchgate.net/publication/227704717>

Line Scan Diffusion Imaging

ARTICLE *in* MAGNETIC RESONANCE IN MEDICINE · OCTOBER 1996

Impact Factor: 3.57 · DOI: 10.1002/mrm.1910360403 · Source: PubMed

CITATIONS

211

READS

35

6 AUTHORS, INCLUDING:



Hákon Gudbjartsson Ph.D

deCODE genetics, Inc.

4 PUBLICATIONS 325 CITATIONS

SEE PROFILE



Istvan Akos Morocz

Harvard Medical School

37 PUBLICATIONS 1,075 CITATIONS

SEE PROFILE



Samuel Patz

Harvard Medical School

127 PUBLICATIONS 4,490 CITATIONS

SEE PROFILE



Ferenc A Jolesz

Harvard Medical School

671 PUBLICATIONS 41,045 CITATIONS

SEE PROFILE

Line Scan Diffusion Imaging

Hákon Gudbjartsson, Stephan E. Maier, Robert V. Mulkern, István Á. Mórocz, Samuel Patz, Ferenc A. Jolesz

A novel line scan diffusion imaging sequence (LSDI) is introduced. LSDI is inherently insensitive to motion artifacts and high quality diffusion maps of the brain can be obtained rapidly without the use of head restraints or cardiac gating. Results from a stroke study and abdominal diffusion images are presented. The results indicate that it is feasible to use the LSDI technique for clinical evaluation of acute ischemic stroke. In contrast to echo-planar diffusion imaging, LSDI does not require modified gradient hardware and can be implemented on conventional scanners. Thus, LSDI should dramatically increase the general availability of robust clinical diffusion imaging.

Key words: diffusion imaging; line scan; LSDI, stroke imaging.

INTRODUCTION

NMR has been used to study water self-diffusion (1) for several decades but only in recent years has it been used on a clinical basis for *in vivo* studies. The initial attempts for *in vivo* imaging of diffusion were based on pulsed gradient spin-echo (PGSE) (2, 3) and steady-state free precession (SSFP) (4) sequences. However, both of these techniques are hampered by severe bulk motion artifacts (5) that make them problematic for accurate assessment of the diffusivity *in vivo*. The advent of diffusion-weighted echo-planar imaging (EPI) has made it possible to quantitatively measure diffusion while minimizing physiological motion artifacts (6, 7).

Currently EPI is not a very widespread technique, because of its need for specialized expensive gradient hardware. Furthermore, EPI diffusion images suffer from large field inhomogeneities. This has motivated an ongoing research to find techniques that would allow *in vivo* diffusion studies on conventional MR scanners.

Several approaches have been proposed such as reduction of patient motion with customized head restraints (8). This is generally uncomfortable and inconvenient, especially for patients with head injuries. Also, pulsatile brain motion cannot be eliminated in this way.

The problem of rigid body translational motion in PGSE has also been dealt with by postprocessing techniques. An elegant approach is the use of a "navigator echo" (9, 10). The navigator technique has been extended

to correct for rigid in-plane rotation (11) and recently fast imaging sequences that employ multiple echoes have also been augmented with navigator echoes (12–15). Cardiac gating is crucial to minimize cardiac-induced motion, which is spatially varying (16) and cannot be corrected by using a navigator. Also, in principle corrections for rotation work only when the diffusion sensitivity is applied in the phase encoding direction (11). Hence, reliable diffusion trace or anisotropy maps cannot be obtained with the navigator technique (12). It is important, however, to measure the diffusivity in three orthogonal directions, since cell membranes and other oriented molecular structures lead to anisotropic water displacement. Moreover, anisotropy can be used to determine nerve fiber orientation within brain white matter (17, 18). It also permits the distinction of reduced diffusion in white matter due to acute ischemia from axon orientation-related variations of the diffusion (19, 20).

A technique related to the navigator technique is the spiral scan diffusion sequence (21). This technique uses a phase correction scheme without a separate navigator echo. Because the center of *k*-space is sampled in each shot, the signal from the center of the *k*-space can be used as a reference. Most recently, a reference phase map has been introduced to correct diffusion-weighted images (22). This method is essentially identical with the navigated PGSE technique (10), except that the phase information is acquired in a separate scan.

Another technique that is known to be insensitive to motion artifacts (in terms of ghosting artifacts) is projection reconstruction. This technique has been used for diffusion imaging (23), and a modified version, based on the magnitude of the projections, has been proposed to reduce the motion artifacts (24, 25). However, this technique corrects only for motion in the form of bulk displacement and suffers from signal loss if the motion is spatially varying.

Some of the most recent applications of diffusion imaging are in the abdomen (26) and the heart (27). The functional status of the kidney has been explored by means of the apparent diffusion coefficient (ADC) (28). These studies were done with diffusion-weighted EPI. At present, it seems unlikely that techniques that rely on postprocessing with navigator echoes will become practical in the abdomen, due to the complexity of the motion there.

Approaches that offer good immunity to motion artifacts on conventional scanners are volume- or column-selective NMR. Column or line scan techniques have been used for *in vivo* spectroscopic studies (29), thermal mapping (30), and quantitative flow and diffusion measurements (17, 31–33). 1D profile techniques lack the anatomic details present in 2D methods. Modifications of these 1D techniques to 2D imaging sequences have been

MRM 36:509–519 (1996)

From the Brigham and Women's Hospital, Department of Radiology, Harvard Medical School (H.G., S.E.M., I.A.M., S.P., F.A.J.), Massachusetts Institute of Technology, Department of EECS (H.G.), Children's Hospital, Department of Radiology, Harvard Medical School (R.V.M.), Boston, Massachusetts.

Address correspondence to: Hákon Gudbjartsson, Ph.D., Brigham and Women's Hospital, LMRC, Room 012, 221 Longwood Avenue, Boston, MA 02115.

1996 SMR Young Investigators' Moore Award Finalist

0740-3194/96 \$3.00

Copyright © 1996 by Williams & Wilkins

All rights of reproduction in any form reserved.

proposed in the literature (34–38); however, application to diffusion imaging has not been contemplated.

We have extended the column-selective technique into what we call line scan diffusion imaging (LSDI) (39). With the LSDI technique, we are able to acquire high quality diffusion images in scan times of 30 s. This imaging technique is extremely robust, and diffusion maps of the brain that are essentially free of motion artifacts can be obtained without the use of head restraints or cardiac gating.

In this paper, the basics of the LSDI sequence and its intrinsic properties are described. Moreover, initial results on diffusion imaging of the brain and the abdomen are presented.

METHODS

Line Scan Diffusion Imaging

LSDI uses multiple diffusion-weighted spin-echo column excitations to form a 2D image. As shown in Fig. 1, the basic sequence is composed of spatially selective $\pi/2$ and π pulses. The diffusion gradients can be applied in arbitrary directions and are placed on both sides of the refocusing π pulse, followed by a standard frequency encoding readout along the selected column.

The LSDI image is composed of a series of 1D *magnitude* profiles obtained from parallel columns lying in the image plane. The sequential collection of this line data in independent acquisitions makes the sequence largely insensitive to bulk motion artifacts since no phase encoding is used and shot-to-shot phase variations are fully removed by calculating the magnitude of the signal.

Each column is formed by the intersection of two planes selected by the two-slice selective RF pulses. For the acquisition of one column, the most obvious choice is to select one plane orthogonal to the image plane and the other within the image plane itself (35, 36). In the repetitive process of line acquisition, this procedure leads to

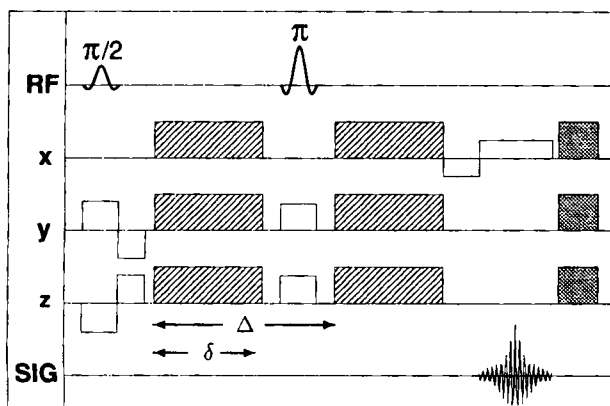


FIG. 1. The basic LSDI sequence diagram. The hatched areas indicate the diffusion gradients; and the shaded areas, the crusher gradients. RF, radiofrequency excitation; x, read-out direction; y and z, select directions; SIG, signal. The amplitude of the crusher gradients varies from shot to shot (38). The diffusion attenuation is given by $\exp(-b \cdot \text{ADC})$, where $b = \gamma^2 G^2 \delta^2 (\Delta - \delta/3)$, γ denotes the gyromagnetic ratio, G is the gradient amplitude, and ADC is the apparent diffusion coefficient.

spin saturation and subsequent tissue-specific T_1 -associated signal loss unless a sufficient period of time between column excitations is permitted. For quantitative diffusion maps composed of 256 lines, this would lead to an unacceptably long residence time in the scanner.

To allow for a faster repetition of the excitation without inflicting spin saturation, the excitation scheme shown in Fig. 2 is used. The basic principle is to avoid an alignment between the planes excited by the selective pulses and the imaging plane. The selected planes are positioned such that the volume at their intersection forms the column of interest in the imaging plane. The angles α and β between the selected planes and the imaging plane (see Fig. 2) can be chosen with a certain degree of freedom.

Interleaving Scheme

Depending on the field of view (FOV), the number of columns (N), and the size of their cross-sections a and b , the selected columns that form the lines in the image, may partially overlap. In this case, spin saturation must be avoided by using an interleaved acquisition scheme as shown in Fig. 3. For a sufficiently large number of lines (see Fig. 2), the time between successive line acquisitions is then restricted primarily by the echo time required for adequate sensitivity to diffusion.

Figure 3 shows an example in which the image plane is covered by $N = 31$ columns and the column step size, s , is 4. The number of columns per sweep is therefore $\lceil N/s \rceil$. Here $\lceil x \rceil$ denotes the smallest integer that is larger or equal to x . Also shown is the order of the acquired columns for each sweep through the image plane.

As shown in Fig. 3, no data are collected during sweep number 0, whereas, in sweep number 4, the columns of sweep number 0 are re-excited and data is acquired. The purpose of this additional sweep is to ensure steady-state magnetization in each column. This is important, when columns overlap and if there is cross-talk due to imperfect slice profiles. It should be noted, that if more than one image, e.g., different b factors, is acquired, this extra

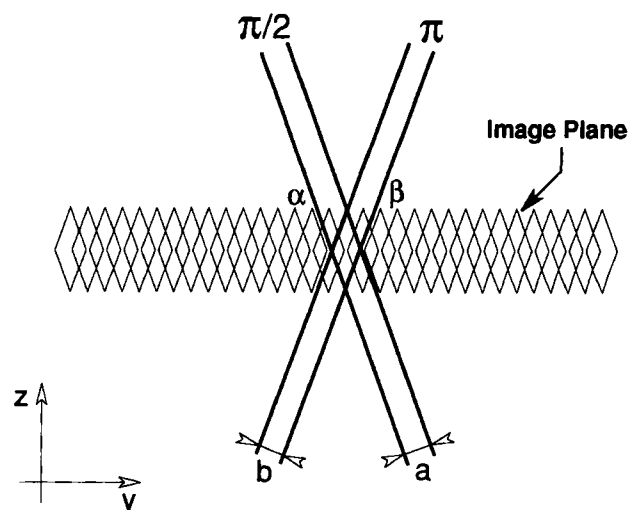


FIG. 2. The selective excitation produced by the LSDI sequence shown in Fig. 1.

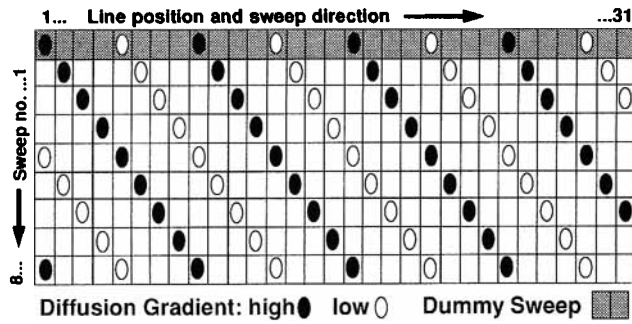


FIG. 3. Interleaved acquisition scheme for a line scan image composed of 31 columns. To reach steady state of the magnetization, the first set of columns is excited with a “dummy sweep” and data is only collected at later excitations. With the interleaving shown here, the repetition time can be reduced by a factor of ca. 8 without increasing spin saturation. The diffusion gradient amplitude alternates between the high and the low state.

sweep needs only to be performed once. The effective repetition time is defined as the time between the excitation of two adjacent columns. For all columns except number 0, it is given by

$$TR_{\text{eff}} = \lceil N/s \rceil \cdot TR \quad [1]$$

Here TR refers to the repetition time of the $\pi/2$ excitation pulses. From Fig. 3, one can conclude that if the number of columns were 32, the effective repetition time of the columns excited in sweep number 4 would be different from the effective repetition time of the other columns. Therefore, we use odd column numbers, e.g., 63, 127, or 255.

Provided that TR_{eff} is long enough, signal loss due to spin saturation is avoided. The column step size, s , is chosen such that $s \times \text{FOV}/N$ becomes larger than the column width. Apart from the time spent on the extra steady-state sweep, the total scan time for one image is given by $N \times TR$.

In the repetitive process of column excitation, the selective π pulses intersect with previous selective $\pi/2$ pulses outside the image plane as shown in Fig. 4a. Particularly, if the diffusion gradients are turned off, this leads to secondary echoes and ultimately to image artifacts. To some extent these echoes can be reduced by crusher gradients after signal readout. The crusher gradient direction is alternated between each excitation (38) to postpone the refocusing of secondary echoes such that T_2 relaxation and diffusion attenuation render them insignificant. By alternating the orientation of the selective pulses, as shown in Fig. 4b, there is an efficient elimination of the strongest secondary echoes that permits a substantial reduction in duration and amplitude of the crusher gradients.

With short repetition times, the heavy use of diffusion gradients can lead to overheating of the gradient amplifiers. To reduce the gradient duty-cycle, we have modified our interleaving scheme such that the sequence alternates between high and low diffusion weighting. Two images, with high and low b factors, are therefore acquired simultaneously. A nice feature of this scheme is that it totally eliminates any secondary echoes. Further-

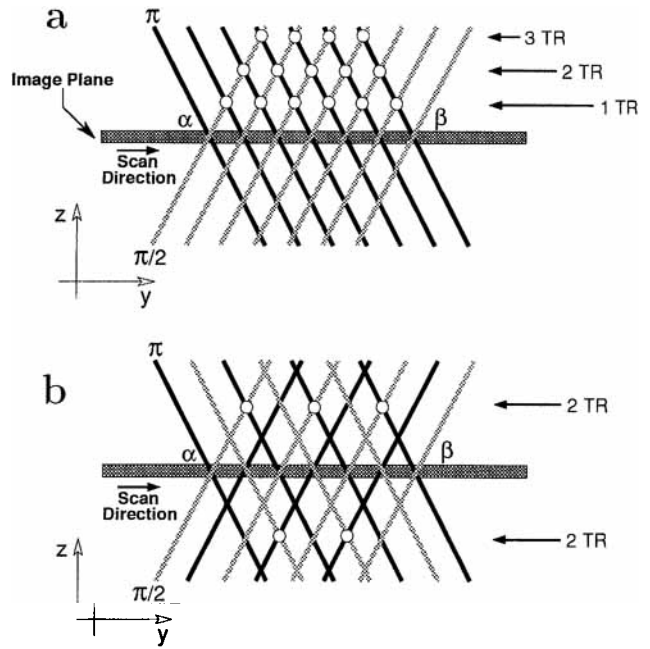


FIG. 4. Two possible arrangements (a) and (b) for the sequence of selective excitations. Selective pulses of $\pi/2$ (gray) and π (black), which define the column in the image plane, are applied sequentially from left to right. The selective π pulse (refocusing pulse) intersects with earlier selective $\pi/2$ pulses, outside the image plane. This produces secondary echoes. The strength of these echoes decreases with the delay (number of repetition time intervals TR) between the selective pulses. With arrangement (a) $\pi/2$ (α) and π (β), for each excitation, all previous $\pi/2$ pulses will contribute to secondary echoes by refocusing after 1 TR , 2 TR , 3 TR , etc. With arrangement (b) $\pi/2$ (α) and π (β), followed by $\pi/2$ (β) and π (α), pulses will contribute to secondary echoes only by refocusing after 2 TR , 4 TR , 8 TR , etc. Thus, every second and particularly the strongest secondary echo (refocusing after 1 TR) is eliminated in arrangement (b).

more, by making the low b factor sufficiently high, FIDs resulting from imperfections in the refocusing pulse are eliminated. Also, the strongest stimulated echo, which because of imperfect slice profiles comes from a large fraction of the image volume, is successfully eliminated by alternating between the high and the low b factor.

The LSDI Point Spread Function

The resolution in the frequency encoding direction (x) along the column is determined as in the standard Fourier imaging techniques (40) by sampling bandwidth, gradient amplitude and duration. Hence, along the column, the shape of the point spread function (PSF) is a sinc function.

For the y and z directions, the PSF is a triangular function that depends on the thickness, a and b , and the angles, α and β , of the selected planes (see Fig. 2). The signal strength is then determined by the cross-sectional area of the columns.

For imaging with overlapping columns, the symmetric solution ($\alpha = \beta$, $a = b$) is advantageous, because most of the signal derives from the central portion of the cross-section. The width of the selected column defines the

in-plane resolution, and the height defines the image slice thickness. The half-maximum of the PSF is used to define the effective resolution. Hence, for the symmetric case, the effective image plane slice thickness can be defined as $a/2\cos\alpha$ and the effective in-plane resolution as $a/2\sin\alpha$.

In 2D spin-warp Fourier imaging, the established ratio between slice thickness and in-plane resolution lies in the range of 2:1 and 4:1. This ensures good resolution of anatomic details under the constraints of signal-to-noise ratio (SNR). As shown in Fig. 5, for a constant cross-sectional area, inclination angles between 65° and 75° produce a similar range of height-to-width ratio. Compared with an inclination at 45° , inclination at 70° improves the in-plane resolution by 40%, without reducing the SNR. Because of the reduced overlap, it is possible to use smaller column step size and therefore longer effective repetition time.

One can argue that overlapping of the columns is favorable because it avoids under-sampling of the image or what is usually referred to as aliasing (41). If the columns overlap substantially, the image can be low-pass filtered to improve the SNR without any significant loss in resolution.

Signal-to-Noise Considerations

One of the main disadvantages of a line-scan technique is the inherently low SNR. In the LSDI technique, a single column contributes to the NMR signal as opposed to regular 2D spin-warp Fourier imaging (40) in which the signal originates from a complete slice. Because of the inherently low SNR of the LSDI sequence, the SNR issue is of great importance. The problem of SNR in MRI has

been treated before by several authors, e.g., refs. 42 and 43.

For a simplified comparison of the SNR of the line scan and the 2D spin-warp technique, the same slice thickness is assumed for both. The effective column width, CW, is then defined as the ratio of the cross-sectional area and the slice thickness. By this definition, the actual slice thickness becomes irrelevant.

Consider an "ideal" uniform phantom that extends over the whole field of view. The signal received from each LSDI column excitation is proportional to the column width and the standard deviation of the noise is denoted by σ . With Fourier encoding, only the zero phase encoding line ($k_y = 0$) gives a non-zero NMR signal, with an amplitude proportional to the FOV. For this particular phantom, other k lines contain only noise; the same as in the LSDI case. This is because, the Fourier transform of this phantom is a sinc function with its zeros located in k -space where the k lines are acquired. The total noise in the Fourier image will depend on the number of k lines, i.e., the image resolution N . The noise standard deviation in the Fourier image is the square root of the total noise variance, $\sigma^2 N$. For this particular phantom, we can therefore write

$$\frac{\text{SNR}_{\text{LSDI}}}{\text{SNR}_{\text{FOV}}} = \frac{\text{FOV}/\sqrt{\sigma^2 N}}{\text{CW}/\sigma} = \sqrt{\frac{\text{FOV}}{\text{CW}}} = \sqrt{N} \quad [2]$$

Here the same spatial resolution is assumed in both imaging techniques, i.e., $N = \text{FOV}/\text{CW}$. It turns out that Eq. [2] holds for any phantom, given that N is high enough, such that all the significant spatial frequencies of the phantom are acquired. Equation [2], however, ignores the fact that for short repetition times, the influence of relaxation is different in the two methods. In the LSDI technique, it is the effective repetition time that will determine the steady-state longitudinal magnetization. For very small SNR, the bias due to the Rician distribution of the magnitude data has to be considered (44, 45).

Optimized Diffusion Gradient Scheme

Two images with different diffusion weighting are needed to assess the diffusion coefficient in the direction of the diffusion gradient. Because of the microscopic structure of tissues, the diffusion is anisotropic, and measurements in three orthogonal directions must be obtained to acquire an isotropic diffusion map (trace of the diffusion tensor) (18) and information about diffusion anisotropy. To date, this has been done by measuring the diffusion along the MR imager gradient coil principal axes, \hat{x} , \hat{y} , and \hat{z} . Simultaneous use of all three gradients results in a considerably higher gradient amplitude. If the maximal relative gradient amplitude in \hat{x} , \hat{y} , and \hat{z} direction is equal, we define a new orthogonal coordinate system as

$$\begin{aligned} \hat{x}' &= -\hat{x} + \hat{y} - \hat{z}/2 \\ \hat{y}' &= \hat{x} + \hat{y}/2 - \hat{z} \\ \hat{z}' &= \hat{x}/2 + \hat{y} + \hat{z} \end{aligned} \quad [3]$$

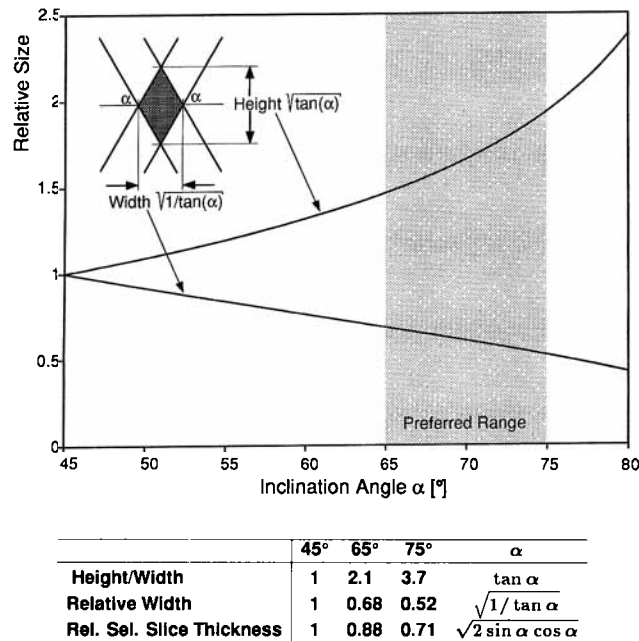


FIG. 5. Relation between the inclination angle and the height and width of columns for a constant cross-sectional area. With inclination angles between 65° and 75° , the height-to-width ratio of the columns is comparable with the optimal height-to-width ratio of volume elements in conventional imaging.

The reader can verify that \hat{x}' , \hat{y}' , and \hat{z}' are mutually orthogonal. Furthermore, this choice of axis gives the maximum gradient strength for three orthogonal directions, $G_{x'}$, $G_{y'}$, and $G_{z'}$. An identical diffusion gradient scheme has been derived independently by other researchers (46) and a similar tetrahedral encoding scheme has recently been published (47). The amplitude gain is 50% compared with using the conventional gradient axes. For a given diffusion sensitivity, the duration and ultimately the echo time can be reduced by approximately one fourth because the effect of the diffusion gradients is proportional to the square of their amplitude and the cube of their duration. The disadvantage of using this modified gradient axis is that they no longer coincide with the principal axis of the image. For diffusion tensor trace and anisotropy maps, this does not pose any problems, since the trace is rotation invariant.

The diffusion weighting is determined by the b factor as shown in Fig. 1. The signal attenuation is then described as $S(b) = S(0) \exp(-b \cdot \text{ADC})$. The apparent diffusion coefficient can be estimated as the slope of a linear least-squares fit to the logarithm of the signal amplitude acquired with two different b values, e.g., low and high b factors. The precision of the estimated diffusion coefficient depends on the choice of the b factors. As mentioned earlier, the low b factor is made sufficiently large such that the FID resulting from the imperfect refocusing pulse is eliminated. This also minimizes the signal contribution from intravascular spins. The optimal high b factor was found by computer simulation. The computer model considers the influence of the maximum gradient strength ($0.01 \text{ T/m} = 1 \text{ G/cm}$) on the echo time and the transverse relaxation in brain tissue ($T_2 \approx 80 \text{ ms}$ for gray and white matter). The figure of merit is the average precision in the estimates of the diffusion coefficients, in the range from 0.1 to $1 \mu\text{m}^2/\text{ms}$. The results indicate that the optimum b factor for brain diffusion maps is close to 750 s/mm^2 (45). However, the improvement in the precision is minimal as b exceeds 500 s/mm^2 .

When many averages are used, the polarity of the diffusion gradients is alternated, to reduce the effect of cross-terms from the imaging and slice-selective gradients (33). Averaging must be done after calculating the magnitude of the signal to avoid introducing sensitivity to phase variations.

Optimized Receiver Bandwidth

The optimum bandwidth is found by maximizing the SNR of the spin echo with respect to the sampling period. Because most of the signal energy comes from low spatial frequencies, the SNR criteria can be written by maximizing the ratio of the signal to the noise at the center of k -space. During the acquisition of the data points that are sampled before reaching the center of k -space, i.e., $N_x/2$ points, the signal is attenuated by transverse relaxation. Also, an equal time period is added to the time between the $\pi/2$ and the π pulse to ensure a full spin echo in the middle of the acquisition period. The noise is inversely proportional to the square root of the sampling period, T .

We therefore get

$$T_{\text{opt}} \approx \arg \max_T \left\{ \exp\left(-\frac{TN_x}{T_2}\right) \sqrt{T} \right\} = \frac{T_2}{2N_x} \quad [4]$$

Note that with this optimal sampling period, the intrinsic spectral broadening due to T_2 relaxation [48, p. 185] is not a problem, because it is smaller than the bandwidth per voxel, i.e., $(1/T_{\text{opt}})/N_x = 2/T_2 > 1/\pi T_2$. The PSF will be similar to the regular sinc function but with smaller sidelobes. With 128 samples in the frequency encoding direction, this indicates that the optimal bandwidth for brain imaging is in the range from 1.2 to 2.4 kHz. Note that here the bandwidth refers to half of the frequency passband, i.e., $\text{BW} = 1/2T$. This low bandwidth makes the image very sensitive to field inhomogeneities and chemical shift distortions. For most of our studies on a 1.5 T system, we used either 8 or 4 kHz bandwidth. At lower field strength, a reduced bandwidth can be used, since distortions from field inhomogeneities and chemical shift scale with field strength. In preliminary experiments on a 0.5 T system, we found that 2 kHz bandwidth gives a good compromise between SNR and short repetition time (45).

RESULTS

The LSDI sequence described in the previous section was implemented on a 1.5 T GE Signa whole body scanner (General Electric Medical Systems, Milwaukee, WI) equipped with the 5.4 operating system and standard gradient hardware with a maximum gradient strength of 1 G/cm. The images were reconstructed on-line with the Signa software. Diffusion and anisotropy maps were calculated off-line.

Phantom Studies

To verify the diffusion sensitivity of the LSDI sequence, the diffusion coefficient of doped water in a phantom was measured at room temperature in all three directions, \hat{x}' , \hat{y}' , and \hat{z}' . The b factor was stepped through the values of 5, 105, 205, 305, 405, and 505 s/mm^2 . For each b factor, an LSDI image was acquired and the average signal intensity was determined within a region of interest (ROI). For each b factor, two images were acquired with opposite polarities on the diffusion gradients, as described in the end of the previous section. The results are shown in Fig. 6. The logarithm of the signal as a function of b fits very well to a straight line. The least-squares fit yielded the following diffusion coefficients: $D_{x'} = 1.82 \mu\text{m}^2/\text{ms}$, $D_{y'} = 1.80 \mu\text{m}^2/\text{ms}$, and $D_{z'} = 1.78 \mu\text{m}^2/\text{ms}$. For comparison, when only a single polarity on the diffusion gradients was used, the best fits were: $D_{x'} = 1.78 \mu\text{m}^2/\text{ms}$, $D_{y'} = 1.82 \mu\text{m}^2/\text{ms}$, and $D_{z'} = 1.84 \mu\text{m}^2/\text{ms}$. The relative precision of the averaged ROIs was from 0.06–0.17%; hence, the precision of the estimates is $0.0026 \mu\text{m}^2/\text{ms}$. Therefore, difference in the estimates of the diffusion coefficients has to be associated with background gradients, cross-terms, and nonidealities in the gradients or small temperature variations.

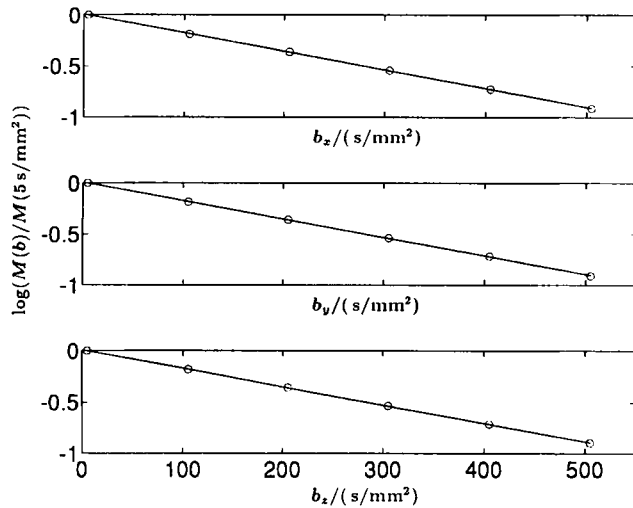


FIG. 6. The logarithm of the signal diffusion attenuation of doped water plotted against the b -factor. The diffusion sensitivity is in direction x (top), y (middle), and z (bottom). The circles represent the means of the ROIs, and the lines show the least-square linear fit.

Diffusion Imaging of the Brain

To demonstrate the quality and the precision of the LSDI technique, we acquired coronal ADC maps of a healthy volunteer. No cardiac gating or head constraints were used. The slice selective pulses were chosen such that $a = b = 5$ mm, $\alpha = \beta = 70^\circ$ (see Fig. 5). With this setting the effective slice thickness is approximately 7 mm. The FOV was set to 24 cm and the repetition time used was 130 ms. The total number of columns was 255 and the column step size, s , was 16 yielding an effective repetition time of 2.1 s. The total acquisition time for each image in Fig. 7 was approximately 33 s. For all six images used to calculate the ADC trace, the total scan time was 3.5 min. The resolution in the frequency encoding direction was set to 128 sample points with a bandwidth of 8 kHz. For each direction of the diffusion sensitivity, two b

factors were used: 5 and 505 s/mm^2 . The echo time (TE) was 85 ms. Figure 8 shows the resulting ADC-trace map.

To estimate the precision of the ADC map, the acquisition described above was repeated three more times such that four independent ADC maps could be calculated. A large ROI was defined, which included the whole brain, and for each image pixel we calculated the mean, $M_D = \sum_{i=1}^4 D_i/4$, and the variance, $\sigma_D^2 = \sum_{i=1}^4 (D_i - M_D)^2/3$. The mean standard deviation of the whole ROI was found to be $\sigma_D = 0.077 \mu\text{m}^2/\text{ms}$. Similarly, the mean relative precision, σ_D/M_D , was calculated and found to be 6%. From two of the four ADC maps, a scatter diagram was produced as shown in Fig. 8. In the scatter diagram, each pixel in the ROI is given a coordinate according to the two independent ADC maps. Ideally, all the pixels should fall on a straight diagonal line, but due to image noise and possible motion between the two acquisitions, the pixels are spread around the diagonal line.

Acute Stroke Patient

Figure 9 shows the first clinical LSDI images. A 45-year-old female patient was imaged 8 h after an acute stroke. Imaging parameters were identical with those used to obtain Fig. 7. Minimal head restraints were used with no cardiac gating. The lesion is clearly identified on the diffusion-weighted images but hardly seen on the highly T_2 -weighted images (those with low b).

Figure 10 shows the three orthogonal ADC maps and the corresponding anisotropy map that is calculated from the standard deviation of D_x , D_y , and D_z (20). This does not give a true rotationally invariant anisotropy map since this definition neglects off-diagonal terms in the diffusion tensor (47), but, fewer measurements are needed for its calculation and it never overestimates the anisotropy. The anisotropy map is inherently much more noisy than the ADC trace map; however, one can see that anisotropy is highest in the white matter.

An ADC trace map was calculated from the three orthogonal diffusion maps and shown in Fig. 11. Notice the

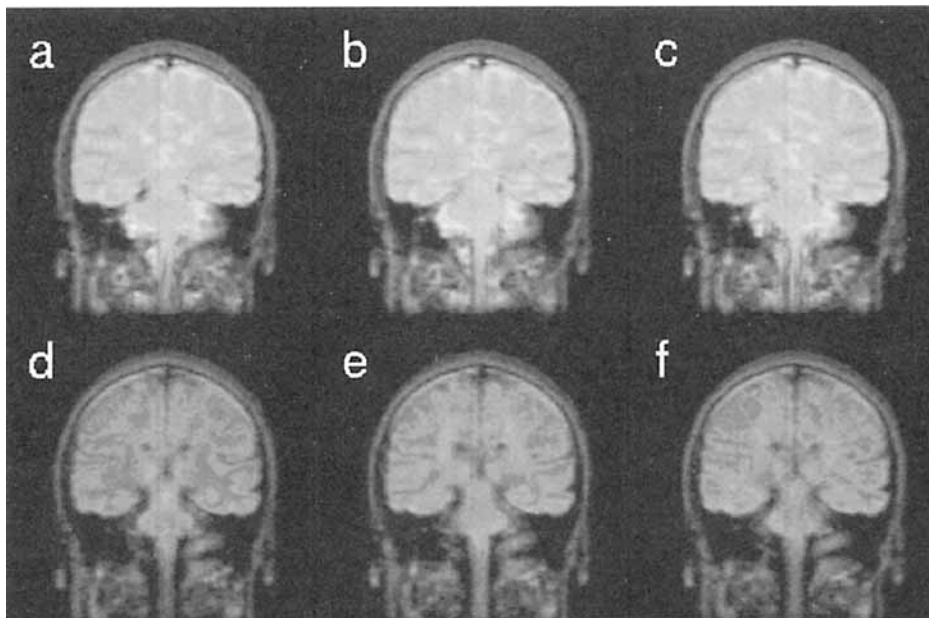


FIG. 7. Coronal images of a healthy volunteer. FOV = 24 cm, $TR = 130$ ms, $a = b = 5$ mm, $\alpha = \beta = 70^\circ$ (see Fig. 5), 255 columns, 8 kHz bandwidth, $TR_{\text{eff}} = 4.2$ s, $TE = 85$ ms. (a) $b_x = 5 \text{ s/mm}^2$. (b) $b_y = 5 \text{ s/mm}^2$. (c) $b_z = 5 \text{ s/mm}^2$. (d) $b_x = 505 \text{ s/mm}^2$. (e) $b_y = 505 \text{ s/mm}^2$. (f) $b_z = 505 \text{ s/mm}^2$.

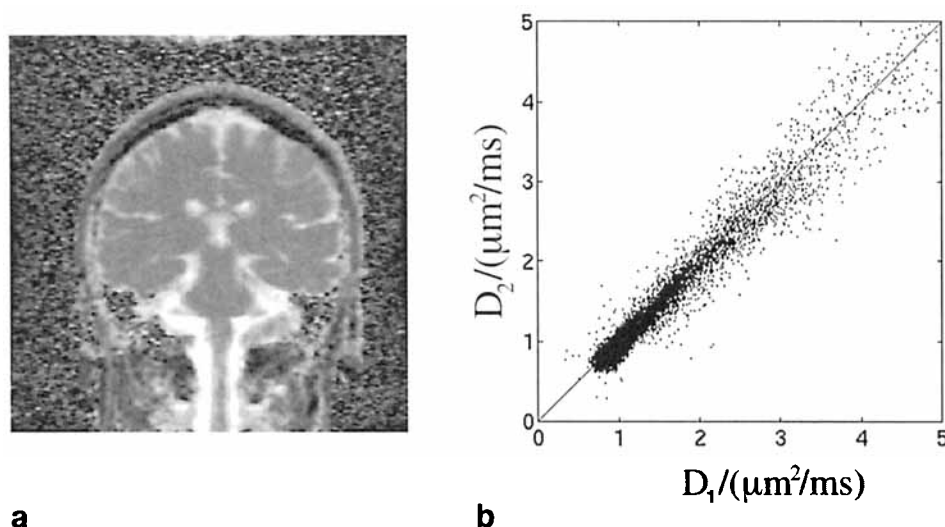


FIG. 8. (a) Coronal ADC trace map produced from the images in Fig. 9. Relative precision in the ADC trace map is 6%. (b) A scatter diagram in which each pixel in the brain is given a coordinate according to the two independent ADC maps. Ideally, all the pixels should fall on a straight diagonal line.

nonlinear gray scale, used to emphasize the variations in the diffusion map. This gray scale is adopted from histogram equalization (49) of brain diffusion maps. For comparison, a T_2 -weighted fast spin-echo image (FSE) of the same plane is shown. Almost no abnormalities are visible on this image. The images on the right side, which were acquired 4 days after the stroke onset, show a larger area of reduced ADC and increased T_2 on the diffusion map and the FSE image, respectively.

Reduced Imaging Time and Bandwidth

In previously shown images, the number of columns was always 255 and the bandwidth was 8 kHz. By lowering the bandwidth to 4 kHz and reducing the column number to 127, imaging time is halved without sacrificing SNR (45). Image distortions from chemical shift and field inhomogeneities become more conspicuous however. Figure 12 shows images with low diffusion weighting and 4 kHz bandwidth. A slight displacement between the skull

and the brain along the column direction is visible. Both image sets were processed in the same way, except that the 127 columns were extrapolated into 255 columns.

These results show that the LSDI technique is capable of producing high quality images in 20 s per image. A full ADC trace map can therefore be acquired in less than 2 min per slice. Furthermore, the region of interest can often be covered by using a rectangular field of view, e.g., 3/4 FOV in brain imaging. In such situations, the imaging time can be made even shorter.

Diffusion Imaging of the Abdomen

Figure 13 shows coronal images of a healthy volunteer. The slice selective pulses were chosen such that $a = b = 1$ cm and $\alpha = \beta = 70^\circ$ (see Fig. 4). The field of view was set to 40 cm and the repetition time was 150 ms. The total number of columns was 255 and the column step size was 16. The effective repetition time was therefore 2.4 s. To get high SNR, the bandwidth was set to 4 kHz. The

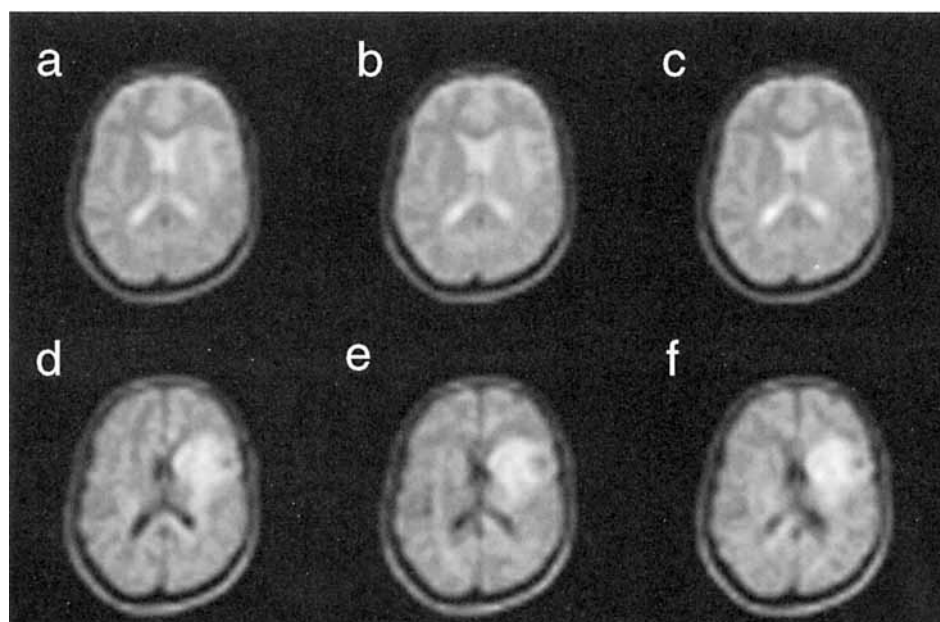


FIG. 9. Acute stroke 8 h after onset. Images of a 45-year-old female stroke patient with different diffusion weighting. Minimal head restraints were used and no cardiac gating. Imaging parameters were identical with those used to obtain Fig. 7. (a) $b_x = 5$ s/mm². (b) $b_y = 5$ s/mm². (c) $b_z = 5$ s/mm². (d) $b_x = 505$ s/mm². (e) $b_y = 505$ s/mm². (f) $b_z = 505$ s/mm².

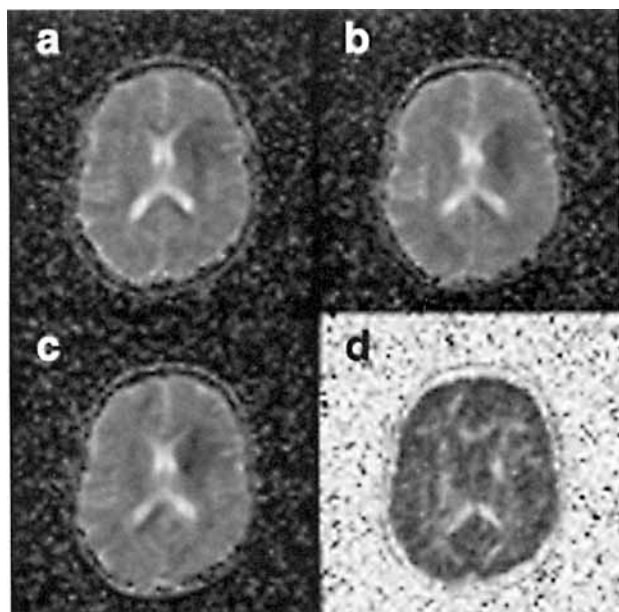


FIG. 10. Acute stroke 8 h after onset. (a) ADC-x. (b) ADC-y. (c) ADC-z. (d) Diffusion anisotropy map.

image quality is still quite good, although some chemical shift distortion is visible, e.g., in the spine. Neither breath-hold nor cardiac gating was used. Note how the fat signal shows practically no change with increased diffu-

sion weighting due to the low diffusion coefficient of high molecular weight triglycerides.

DISCUSSION

In this paper, we have presented and analyzed the LSDI sequence, which is a novel diffusion imaging technique (39). A similar diffusion imaging technique has been presented simultaneously by other researchers (50) as well. However, their technique shows more resemblance with an older technique, called rapid line scan (RLS) or interleaved line scan (ILS), suggested for the imaging of moving objects (37, 38, 51). Common to LSDI and the RLS/ILS techniques is the use of two-slice selective pulses to form columns and the use of time-varying crusher gradients to destroy spurious echoes. There are several technical differences that distinguish the LSDI and the RLS/ILS techniques. In the LSDI sequence, a presweep is used to ensure steady-state magnetization across the whole field of view. Also, in the LSDI image neighboring columns overlap. This avoids aliasing and improves image quality. In the LSDI sequence, the novel idea of alternating the amplitude of the diffusion gradients and the slice selection direction is used with the distinct advantage of reducing spurious echoes. Furthermore, we show that the inclination angle of 45° , used in the RLS/ILS techniques, is outside the optimal range from 65° to 75° . For these reasons, the diffusion images

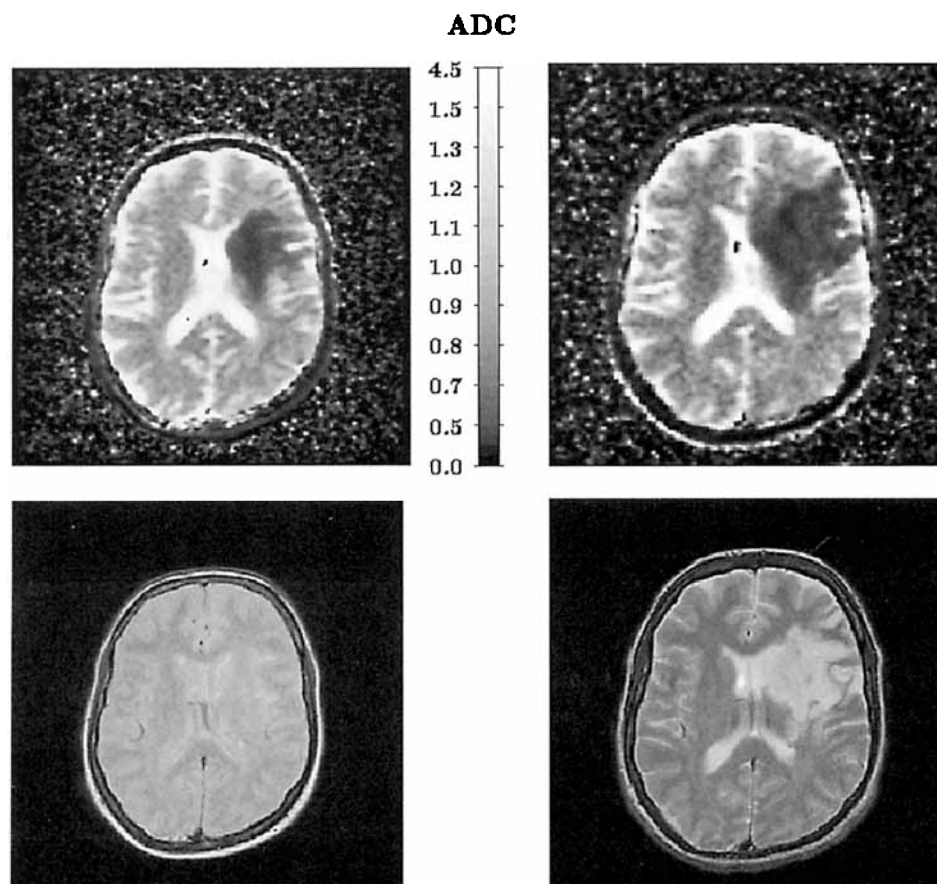


FIG. 11. Acute stroke. (Left) 8 h after onset. FOV = 24 cm. (Right) 4 days after onset. FOV = 22 cm. (Above) ADC trace map. Notice the nonlinear gray scale which is adapted from histogram equalization of brain diffusion maps. The ADC is in units of $\mu\text{m}^2/\text{ms}$. (Below) Fast spin-echo image of the same slice with an effective echo time of 68 ms.

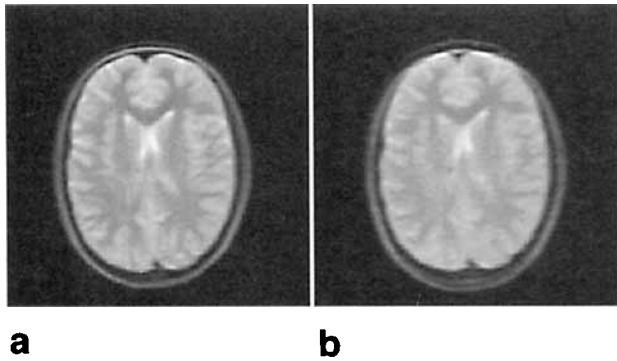


FIG. 12. FOV = 24 cm, $TR = 150$ ms, $a = b = 5$ mm, $\alpha = \beta = 70^\circ$ (see Fig. 5), and $b_x = 5$ s/mm². (a) 255 columns, 8 kHz bandwidth, $TR_{\text{eff}} = 4.8$ s, $TE = 85$ ms. (b) 127 columns, 4 kHz bandwidth, $TR_{\text{eff}} = 2.4$ s, $TE = 90$ ms.

presented here are of greatly improved quality and resolution.

One can argue that diffusion imaging is the ideal application for line scan imaging. The use of long echo times and strong alternating diffusion gradients totally eliminates signal contribution from spins outside the columns, i.e., the secondary echoes. Also, because each echo has self-contained information, the line scan imaging technique gets rid of the major problem associated with diffusion imaging, namely, motion-related phase variations. As long as the motion can be considered uniform within the image voxel and the total tissue displacement small compared with the size of the voxel, the LSDI signal should not be affected. Therefore, to avoid motion artifacts, it is sufficient to have uniform motion within a single image voxel instead of requiring uniform motion within the whole field of view such as for the navigator techniques and diffusion-weighted projection reconstruction. Obviously, the latter is much easier to achieve.

It is shown in Figs. 9–11 that LSDI images can clearly identify the ischemic area in the early phase of acute stroke, whereas it is hardly visible on the T_2 -weighted images (FSE and those with low b). Because LSDI offers high precision diffusion maps, it is possible to accurately monitor the area of reduced ADC. By comparing images

at different time points (Fig. 11), we see that the area of reduced ADC increases with time from stroke onset. Four days after onset of the acute stroke, the ischemic injury becomes more visible on the T_2 -weighted image. These findings agree well with previously published studies on stroke (19, 20, 52). Thus, LSDI has the potential to make patient stroke studies practical with conventional MR scanners.

In contrast to navigated diffusion imaging, LSDI is inherently immune to bulk motion artifacts. For imaging tissues other than heart muscle, the LSDI sequence does therefore not require cardiac gating, which facilitates the technique in the clinical setting. For single slice imaging, the LSDI technique is faster than the navigated PGSE technique. Moreover, unlike the navigated PGSE imaging technique, LSDI does not restrict the diffusion sensitivity to selected spatial directions, which allows accurate assessment of the diffusion tensor trace and anisotropy maps.

The insensitivity of LSDI to bulk motion and susceptibility inhomogeneities makes it applicable for diffusion imaging in the abdomen and the heart. Unlike echoplanar diffusion imaging, it does not require any special gradient hardware. Furthermore, arbitrary oblique imaging planes can be defined without any image distortion. In contrast, when oblique imaging planes are defined in EPI, one has to compromise between susceptibility artifact and Maxwell image distortion (53). In abdominal imaging with a large field of view and severe field inhomogeneities, this may become an issue.

Our initial abdominal diffusion images in Fig. 13b show signal loss in some of the columns. This is because of respiratory motion that causes nonuniform motion within each image voxel. When there is nonuniform motion within each image voxel, the phase dispersion will exaggerate the apparent diffusion attenuation. If the phase distribution is known, its influence can be determined from the LSDI PSF (54). By using small voxels, the influence of phase dispersion can be minimized at the cost of reduced SNR. A better way to reduce motion artifacts in the abdomen is to use breath-hold imaging. Currently, we have not implemented breath-hold imag-

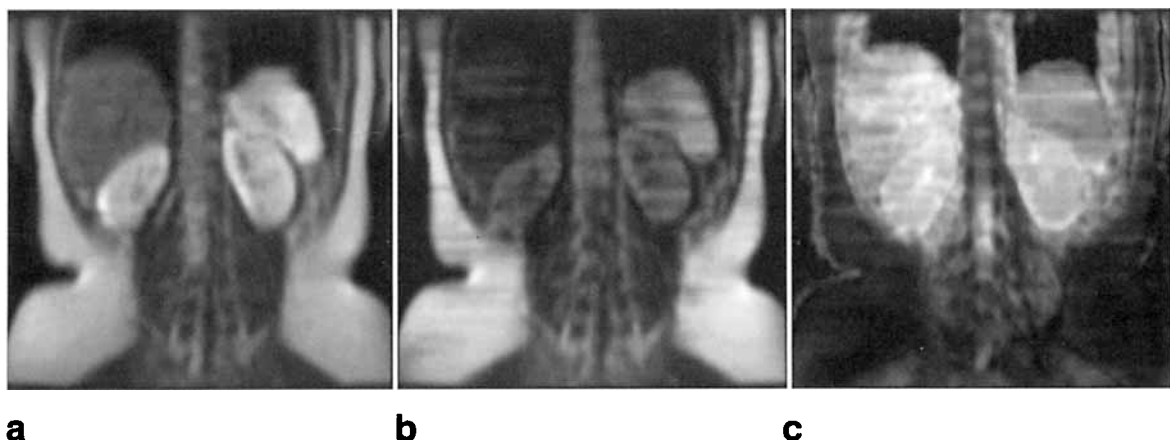


FIG. 13. FOV = 40 cm, $TR = 150$ ms, $a = b = 10$ mm, $\alpha = \beta = 70^\circ$ (see Fig. 5). 255 columns, 4 kHz bandwidth, $TR_{\text{eff}} = 2.4$ s, $TE = 90$ ms. (a) $b_x = 5$ s/mm². (b) $b_x = 505$ s/mm². (c) ADC trace map calculated from six images.

ing; however, this should be straight forward because with LSDI two images can easily be acquired in a single breath-hold. The abdominal diffusion maps compare well with recently published diffusion maps obtained with EPI (26).

In terms of acquisition speed, the LSDI technique is most competent in single slice imaging. However, volume acquisition can be performed by subsequent acquisition of several image planes. Such volume imaging should be practical with the LSDI technique. Because the SNR does not decrease with a reduced field of view in the y direction, it is possible to cover a volume of interest (e.g., the heart muscle) more efficiently with several rectangular fields of view.

CONCLUSION

We have introduced LSDI, which is a new diffusion imaging sequence for conventional MR scanners. Our results show that high quality diffusion images can be acquired rapidly with the LSDI sequence. LSDI is inherently insensitive to motion artifacts, and for brain imaging neither head restraints nor cardiac gating is needed. Hence, it should be very useful for stroke evaluation on conventional scanners.

ACKNOWLEDGMENTS

The authors thank Dr. Koichi Oshio for assistance with the pulse-sequence programming and Dr. Keith Johnson and Dr. Reisa Sperling for help with the patient imaging.

REFERENCES

1. E. O. Stejskal, J. E. Tanner, Spin diffusion measurements: spin echoes in the presence of a time-dependent field gradient. *J. Chem. Phys.* **42**, 288–292 (1965).
2. D. Le Bihan, E. Breton, A. Syrota, Imagerie de diffusion par résonance magnétique nucléaire. *C.R. Acad. Sci.* **301**, 1109–1112 (1985).
3. D. Le Bihan, E. Breton, D. Lallemand, P. Grenier, E. A. Cabanis, M. Laval-Jeantet, MR imaging of intravoxel incoherent motions: application to diffusion and perfusion in neurologic disorders. *Radiology* **161**, 401–407 (1986).
4. D. Le Bihan, R. Turner, J. R. MacFall, Effects of intravoxel incoherent motions (IVIM) in steady-state free precession (SSFP) imaging: application to molecular diffusion imaging. *Magn. Reson. Med.* **10**, 324–337 (1989).
5. H. Gudbjartsson, S. Patz, Simultaneous calculation of flow and diffusion sensitivity in SSFP. *Magn. Reson. Med.* **34**(4), 567–579 (1995).
6. H. R. Avram, L. E. Crooks, Effect of self-diffusion on echo-planar imaging, in "Proc., SMRM, 7th Annual Meeting, Berkeley, CA, 1988," p. 80.
7. R. Turner, D. Le Bihan, J. Maier, R. Vavrek, L. K. Hedges, J. Pekar, Echo-planar imaging of intravoxel incoherent motions. *Radiology* **177**, 407 (1990).
8. D. Chien, K. Kwong, D. Gress, F. Buonanno, R. Buxton, B. Rosen, MR diffusion imaging of cerebral infarction in humans. *AJNR* **13**, 1097 (1992).
9. R. L. Ehman, J. P. Felmlee, Adaptive technique for high-definition MR imaging of moving structures. *Radiology* **173**, 255 (1989).
10. R. J. Ordidge, J. A. Helpert, Z. X. Qing, R. A. Knight, V. Nagesh, Correction of motional artifacts in diffusion-weighted MR images using navigator echoes. *Magn. Reson. Imaging* **12**, 455–460 (1994).
11. A. W. Anderson, J. C. Gore, Analysis and correction of motion artifacts in diffusion weighted imaging. *Magn. Reson. Med.* **32**, 379–387 (1994).
12. A. J. de Crespigny, M. P. Marks, D. R. Enzmann, M. E. Moseley, Navigated diffusion imaging of normal and ischemic human brain. *Magn. Reson. Med.* **33**(5), 720–728 (1995).
13. H. Gudbjartsson, S. Patz, Correction of diffusion weighted RARE images using navigator echoes, in "SMR, 3rd Annual Meeting, Nice, 1995," p. 904.
14. S. Brockstedt, C. Thomsen, R. Wirestam, S. Holtås, F. Ståhlberg, Development of a diffusion-sensitive fast spin-echo pulse sequence with navigator echo motion correction, in "SMR, 3rd Annual Meeting, Nice, 1995," p. 905.
15. K. Butts, A. de Crespigny, M. Moseley, Diffusion-weighted interleaved EPI with navigation for stroke imaging, in "SMR, 3rd Annual Meeting, Nice, 1995," p. 1386.
16. S. E. Maier, C. J. Hardy, F. A. Jolesz, Brain and cerebrospinal fluid motion: real-time quantification with M-mode MR imaging. *Radiology* **193**, 447–483 (1994).
17. T. L. Chenevert, J. A. Brunberg, J. G. Pipe, Anisotropic diffusion in human white matter: demonstration with MR techniques in vivo. *Radiology* **177**, 401–405 (1990).
18. P. J. Basser, J. Mattiello, D. Le Bihan, MR diffusion tensor spectroscopy and imaging. *Biophys. J.* **66**, 259–267 (1994).
19. S. Warach, J. Gaa, B. Siewert, P. Wielopolski, R. R. Edelman, Acute human stroke studied by whole brain echo planar diffusion-weighted magnetic resonance imaging. *Ann. Neurol.* **37**(2), 231–242 (1995).
20. P. van Gelderen, M. H. M. de Vleeschouwer, D. DesPres, J. Pekar, P. C. M. van Zijl, Water diffusion and acute stroke. *Magn. Reson. Med.* **31**(2), 154–163 (1994).
21. T. Tsukamoto, K. King, T. K. F. Foo, E. Yoshitome, Diffusion imaging with spiral scans, in "SMR, 2nd Annual Meeting, San Francisco, 1994," p. 1032.
22. A. M. Uluğ, P. B. Barker, P. C. M. van Zijl, Correction of motional artifacts in diffusion-weighted images using a reference phase map. *Magn. Reson. Med.* **34**, 476–480 (1995).
23. R. V. Mulkern, R. G. S. Spencer, Diffusion imaging with paired CPMG sequences. *Magn. Reson. Imaging* **6**, 623–631 (1988).
24. K. J. Jung, Z. H. Cho, Reduction of flow artifacts in NMR diffusion imaging using new angle tilted line-integral projection reconstruction. *Magn. Reson. Med.* **19**, 349–360 (1991).
25. A. F. Gmitro, A. L. Alexander, Use of a projection reconstruction method to decrease motion sensitivity in diffusion-weighted MRI. *Magn. Reson. Med.* **29**(6), 835–838 (1993).
26. M. F. Müller, P. V. Prasad, B. Siewert, M. A. Nissenbaum, V. Raptopoulos, R. R. Edelman, Abdominal diffusion mapping with use of a whole-body echo-planar system. *Radiology* **190**, 475–478 (1994).
27. R. R. Edelman, J. Gaa, V. J. Wedeen, E. Loh, J. M. Hare, P. Prasad, W. Li, In vivo measurement of water diffusion in the human heart. *Magn. Reson. Med.* **32**, 423–428 (1994).
28. M. F. Müller, P. V. Prasad, D. Bimmler, A. Kaiser, R. Edelman, Functional imaging of the kidney by means of measurement of the apparent diffusion coefficient. *Radiology* **193**, 711–715 (1994).
29. R. V. Mulkern, J. Meng, K. Oshio, C. R. G. Guttman, D. Jaramillo, Bone marrow characterization in the lumbar spine with inner volume spectroscopic CPMG imaging studies. *J. Magn. Reson. Imaging* **4**, 585–589 (1994).
30. C. J. Hardy, H. E. Cline, R. D. Watkins, One-dimensional NMR thermal mapping of focused ultrasound surgery. *J. Comput. Assist. Tomogr.* **18**(3), 476–483 (1994).
31. D. A. Feinberg, P. D. Jakob, Tissue perfusion in humans studied by Fourier velocity distribution, line scan, and echo-planar imaging. *Magn. Reson. Med.* **16**, 280–293 (1990).
32. M. A. Horsfield, G. J. Barker, W. I. McDonald, Self-diffusion in CNS tissue by volume-selective proton NMR. *Magn. Reson. Med.* **31**(6), 637–644 (1994).
33. D. Morvan, In vivo measurement of diffusion and pseudo-diffusion in skeletal muscle at rest and after exercise. *Magn. Reson. Imaging* **13**, 193–199 (1995).
34. A. A. Maudsley, Multiple-line-scanning spin density imaging. *J. Magn. Reson.* **41**, 112–126 (1980).
35. L. E. Crooks, Selective irradiation line scan techniques for NMR imaging. *IEEE Trans. Nucl. Sci.* **27**(3), 1239–1244 (1980).
36. P. L. Davis, L. Kaufman, L. E. Crooks, T. R. Miller, Detectability of hepatomas in rat liver by nuclear magnetic resonance imaging. *Invest. Radiol.* **16**(5), 354–359 (1981).
37. S. Shioya, R. Christman, D. C. Ailion, An in vivo NMR imaging determination of multiexponential Hahn T2 of normal lung. *Magn. Reson. Med.* **16**, 49–56 (1990).

38. D. C. Ailion, K. Ganesan, T. A. Case, R. A. Christman, Rapid line scan technique for artifact-free images of moving objects. *Magn. Reson. Imaging* **10**, 747–757 (1992).
39. H. Gudbjartsson, S. E. Maier, R. V. Mulkern, I. A. Morocz, F. A. Jolesz, Diffusion weighted linescan imaging, in "SMR, 3rd Annual Meeting, Nice, 1995," p. 908.
40. A. Kumar, D. Welti, R. R. Ernst, NMR Fourier zeugmotography. *J. Magn. Reson.* **18**, 69–83 (1975).
41. A. C. Kak, M. Slaney, "Principle of Computerized Tomographic Imaging," IEEE Press, New York, 1988.
42. P. Brunner, R. R. Ernst, Sensitivity and performance time in NMR imaging. *J. Magn. Reson.* **33**, 83–106 (1979).
43. D. L. Parker, G. T. Gullberg, Signal-to-noise efficiency in magnetic resonance imaging. *Med. Phys.* **17**(2), 250–257 (1990).
44. H. Gudbjartsson, S. Patz, The Rician distribution of noisy MRI data. *Magn. Reson. Med.* **34**(6), 910–914 (1995).
45. H. Gudbjartsson, "Magnetic Resonance Imaging of Diffusion in the Presence of Physiological Motion," Ph.D. thesis, Massachusetts Institute of Technology, 1996.
46. A. G. Sorensen, R. M. Weisskoff, T. R. Reese, B. R. Rosen, Optimization of diffusion-weighted MR imaging for evaluation of acute stroke, in "SMR, 3rd Annual Meeting, Nice, 1995," p. 1383.
47. T. E. Conturo, R. C. McKinstry, E. Akbudak, B. H. Robinson, Encoding of anisotropic diffusion with tetrahedral gradients: a general mathematical diffusion formalism and experimental results. *Magn. Reson. Med.* **35**(3), 399–412 (1996).
48. Paul T. Callaghan, "Principles of Nuclear Magnetic Resonance Microscopy," Oxford University Press Inc., New York, 1991.
49. A. K. Jain, "Fundamentals of Digital Image Processing," Prentice Hall, Englewood Cliffs, NJ, 1989.
50. J. De Poorter, Y. De Deene, R. Van de Walle, C. De Wagter, C. Thomsen, S. Brockstedt, F. Ståhlberg, E. Achten, An improved line-scanning technique for in vivo diffusion imaging without motion artifacts, in "SMR, 3rd Annual Meeting, Nice, 1995," p. 907.
51. S. Shioya, R. Christman, D. C. Ailion, A. G. Cutillo, K. C. Goodrich, Nuclear magnetic resonance Hahn spin-echo decay T_2 in live rats with endotoxin lung injury. *Magn. Reson. Med.* **29**(4), 441–445 (1993).
52. M. E. Moseley, J. Kucharczyk, J. Mintorovitch, Y. Cohen, J. Kurhanewicz, N. Derugin, H. Asgari, D. Norman, Diffusion-weighted MR imaging of acute stroke: correlation with T2-weighted and magnetic susceptibility-enhanced MR imaging in cats. *AJNR* **11**, 423 (1990).
53. R. M. Weisskoff, M. S. Cohen, Nonaxial whole-body instant imaging. *Magn. Reson. Med.* **29**(6), 796–803 (1993).
54. V. J. Wedeen, R. M. Weisskoff, B. P. Poncelet, MRI signal void due to in-plane motion is all-or-none. *Magn. Reson. Med.* **32**, 116–120 (1994).